AGU ADVANCING EARTH AND SPACE SCIENCE

JAMES | Journal of Advances in Modeling Earth Systems

RESEARCH ARTICLE
10.1029/2019MS001951

**Key Points:**
- Stratospheric temperature adjustment is an important component of the effective radiative forcing for many greenhouse gases
- The variation of the magnitude and sign of this adjustment with the wavelength at which greenhouse gases absorb is investigated
- The results are used to enhance a widely used simple method for estimating halocarbon radiative efficiency

**Supporting Information:**
- Supporting Information S1
- Supporting Information S2

**Correspondence to:**
K. P. Shine,
k.p.shine@reading.ac.uk

**Citation:**
Shine, K. P., & Myhre, G. (2020). The spectral nature of stratospheric temperature adjustment and its application to halocarbon radiative forcing. *Journal of Advances in Modeling Earth Systems*, *12*, e2019MS001951. https://doi.org/10.1029/2019MS001951

Received 14 NOV 2019
Accepted 17 FEB 2020
Accepted article online 19 FEB 2020



# The Spectral Nature of Stratospheric Temperature Adjustment and its Application to Halocarbon Radiative Forcing

**K. P. Shine**[1] **and G. Myhre**[2]

[1]Department of Meteorology, University of Reading, Reading, UK, [2]CICERO, Oslo, Norway

**Abstract** Stratospheric temperature adjustment (STA) is often a significant component of greenhouse gas radiative forcing (RF), for both the most widely used definition of RF and effective radiative forcing. It is well established that the magnitude and sign of STA differs among greenhouse gases, being negative (at the tropopause) for $CO_2$ increases (because it induces a cooling of the stratosphere) and positive for many halocarbons (because they induce a warming of the stratosphere); this effect is strongly related to the opacity (and hence the effective emitting temperature) of the troposphere at the wavelengths at which gases absorb. Here the spectral variation of STA is examined for the first time by systematically imposing a weak absorber in each of 300 bands of a narrow-band radiation code. For this weak absorber, STA is negative for wavelengths greater than about 13 μm and positive in the 8- to 13-μm "window" except in the vicinity of the 9.6-μm ozone band. By combining narrow-band and line-by-line model results, these findings are used to improve a widely used fast method to estimate radiative efficiency (RE, the RF per unit change in concentration) directly from laboratory measurements or theoretical calculations of halocarbon absorption cross sections; the new method reproduces detailed RE calculations to better than 1.4%. This is a significant improvement over a cruder method used to account for STA in RE tabulations in the Intergovernmental Panel on Climate Change's Fifth Assessment Report, which were used to calculate metrics such as the Global Warming Potential, for halocarbons and related substances.

**Plain Language Summary** Increased emissions and concentrations of greenhouse gases, due to human activity, are a major driver of climate change. Carbon dioxide is the most important such gas, but many other gases are emitted which, collectively, contribute significantly to climate change. This paper focuses on methods to calculate the climate impact of halocarbons which are used in refrigeration, insulation, air conditioning, etc. This includes chlorofluorocarbons (CFCs), whose usage has been phased out because they deplete the ozone layer; hydrochlorofluorocarbons (HCFCs) which were regarded as transitional substances to replace the CFCs; and hydrofluorocarbons, which are widely used replacements for CFCs and HCFCs. It is important to quantify the climate impacts of halocarbons and to compare the relative impact of different halocarbons; this information is used in international agreements aimed at reducing greenhouse gas emissions. This paper presents an important refinement of a widely used simple method for calculating and comparing the climate impact of different halocarbons. This refinement considers the impact of these gases on temperatures in the stratosphere (i.e., altitudes of about 10–50 km); to achieve this, the paper first develops a general understanding of the way such gases influence stratospheric temperatures. The new technique is a significant improvement over previous methods.

## 1. Introduction

Radiative forcing (RF) due to, for example, changes in greenhouse gas concentrations, is a key concept in climate science and indicates the size and sign of drivers of climate change. Specifically, global mean RF is closely related to the resulting global mean surface temperature change. Both the utility and development of the RF concept have been described in several publications (e.g., Myhre et al., 2013; Ramaswamy et al., 2019; Sherwood et al., 2015); successive developments have enabled a more robust relationship between forcing and surface temperature change across a range of different climate change drivers.

The most basic measure is the instantaneous RF (IRF) which computes the irradiance change at the tropopause, due to the driver, in the absence of any other change in the climate system. Calculations of radiative forcing due to changes in greenhouse gas concentrations have, however, long included the impact on

tropopause irradiance of stratospheric temperature adjustment (STA) that occurs in response to those changes. The rationale (e.g., Myhre et al., 2013; Shine et al., 1990) is that RF (which includes STA) is a better predictor of surface temperature response than IRF, at least in simple models; STA is a fast process (timescale of months) compared to the decadal time scale for the surface-troposphere system to respond. This has become the most widely used definition of RF within Intergovernmental Panel on Climate Change (IPCC) assessments and will be the one used here. More recently, it has been recognized that there are additional fast responses to climate change drivers (e.g., in tropospheric temperatures, clouds, and humidity) that occur in the absence of surface temperature change; these are included in the definition of effective radiative forcing (ERF) (Boucher et al., 2013; Myhre et al., 2013; Sherwood et al., 2015), which has been shown in model studies to be an even better predictor of surface temperature response than RF. STA is now one of many rapid adjustments included within ERF, albeit an important one for, for example, $CO_2$ forcing (Smith et al., 2018).

By convention RF has been defined at the tropopause and so indicates the forcing of the surface-troposphere system. The size and sign of STA has long been known to vary among different greenhouse gases (e.g., Myhre & Stordal, 1997; Pinnock et al., 1995). The cooling of the stratosphere in response to increased $CO_2$ concentrations reduces its RF by 10–15%; by contrast, most (but not all—see later) halocarbons lead to a warming of the lower stratosphere that increases their forcing by of order 10%. For some other gases such as $N_2O$ and $CH_4$ (at least when considering their longwave forcing), the impact of STA is much smaller, of order a few percent (e.g., Rind & Lacis, 1993).

The difference in behavior originates from the properties of the greenhouse gas and the extent to which its spectral features overlap with those of other greenhouse gases. A simple conceptual model, which treats the stratosphere as a single emitting and absorbing layer, is now presented, to help interpret the full model simulations presented in later sections. An increase in stratospheric concentrations of a greenhouse gas will increase the emittance of the stratosphere; because of this, if the absorption of radiation by the layer is unchanged, the radiative balance can be maintained at a lower temperature, and so this process acts to cool the stratosphere. The increased stratospheric emittance is also accompanied by an increased absorptance of upwelling radiation from the troposphere—this process, on its own, would lead to a warming of the stratosphere. The net effect is largely determined by the mean altitude (and hence effective emitting temperature) of emission from the troposphere, but it is also likely to depend, to some extent, on the vertical profile of the stratospheric absorption and emission. In relatively opaque spectral regions (e.g., in the vicinity of strong bands of $CO_2$ and water vapor), the upwelling irradiance mostly originates from the upper troposphere. The relatively low effective emitting temperature means that increased stratospheric emission dominates over increased absorption and STA leads to a cooling. This cooling decreases the emission of radiation into the troposphere and so reduces RF. In relatively transparent spectral regions (or in spectral regions where most of the opacity is due to absorption in the lower troposphere), such as across most of the 8- to 13-μm "window," much of the upwelling (clear sky) irradiance originates from the lower troposphere and surface; the high effective emitting temperature means that increased absorption dominates (at least for the lower stratosphere). Hence, STA leads to a warming, which increases RF. Ultimately, as we will show in section 3, the prime determinant of whether the stratosphere cools or warms is the relationship between the radiative forcing at the tropopause and top of atmosphere. As discussed recently by Huang and Wang (2019), the vertical profile of the radiative heating perturbation can be used as a predictor of vertical profile of stratospheric temperature change, and it is possible that such a framework could, in future, be extended to predict the consequent effect on the forcing itself.

This paper presents the first systematic calculation of the impact of STA on RF as a function of the wavelength of absorption for a relatively weak absorber (such as halocarbons at present-day concentrations). This facilitates a clearer understanding of the wavelength dependence of STA. An important practical application of this work is in the computation of the radiative forcing of halocarbons and related gases. Pinnock et al. (1995) introduced a simple and rapid method for the calculation of halocarbon RF that has been widely used by the laboratory and computational spectroscopic communities (e.g., Godin et al., 2019; Papanastasiou et al., 2018). Pinnock et al. (1995) used a narrow-band (10 $cm^{-1}$) radiative transfer model (NBM) to calculate IRF (i.e., neglecting STA) at the tropopause as a function of wavenumber for a hypothetical weak absorber which absorbs equally at all wavelengths. By multiplying the resulting function by the wavenumber-dependent

absorption cross section of a given halocarbon, the (instantaneous) radiative efficiency (i.e., RF per ppb, henceforth RE) could be computed to better than 1% accuracy for a wide range of halocarbons, relative to detailed calculations with the same NBM.

Hodnebrog et al. (2013) updated the calculations of Pinnock et al. (1995), using a line-by-line code to generate the IRF at 1 $cm^{-1}$ resolution and applied the technique to calculate the RE of more than 200 compounds. These were subsequently used to calculate the Global Warming Potentials and Global Temperature change Potentials for these compounds, in the IPCC's Fifth Assessment Report (Myhre et al., 2013). One important advantage of using a common method for calculating RE for this group of gases (compared to the use of REs calculated by different studies using different radiative transfer codes) is that the relative differences in the REs among these gases should be more robust.

Hodnebrog et al. (2013) included a crude approximation for STA by increasing the instantaneous RE by 10% for most gases; exceptions were for CFC-11, CFC-12, HFC-41, and $CF_4$ for which explicit calculations of STA using the Oslo line-by-line model (see section 5) were performed, and HCFC-123, for which a 6.5% adjustment was made based on STA results from the prior literature. The 10% increase for STA was recognized to be a reasonable assumption for many gases, but with notable outliers.

The inclusion of STA in the Pinnock et al. (1995) method then allows its wider applicability to all halogenated and related gases, at no extra computational cost to the user. While in the long term it would be desirable to compute the full ERF of these species, this is not yet possible. The primary reason is that there is a reliance on general circulation models (GCMs) to compute rapid adjustments making it a formidable task to compute ERF for such a wide variety of molecules, especially at their current concentrations; for many gases, internal variability of GCMs would likely swamp the forcing (e.g., Forster et al., 2016) and necessitate long integrations to obtain a reliable signal. In addition, GCM radiation codes typically include only a few halocarbons and have insufficient spectral resolution to fully capture the differences among gases. STA is currently the only rapid adjustment for which there is an accepted methodology which can be applied without recourse to a GCM and that can be implemented in more detailed radiation codes.

After introducing the methodology in section 2, section 3 presents results showing the spectral dependence of STA. Section 4 shows how the Pinnock et al. (1995) method can be adapted to include STA and demonstrates that the method works well for a range of molecules and represents a significant improvement over earlier methods. Section 5 then combines the STA method with updated line-by-line calculations to produce a new set of values for the Pinnock et al. (1995) method. Hence, section 3 focuses more on the underlying physics that enables the development of the technique, while sections 4 and 5 focus on the specific application of the technique to halocarbons and related molecules.

## 2. Radiative Transfer Model

The core of the radiative transfer calculations here use an updated version of the 300-band NBM of Shine (1991) which has a 10 $cm^{-1}$ resolution over the wavenumber domain 0–3,000 $cm^{-1}$. Spectral line parameters are taken from the HITRAN 2016 database (Gordon et al., 2017) with the total internal partition sums from Gamache et al. (2017). The NBM uses the most recent version of the MT_CKD (Mlawer-Tobin_Clough-Kneizys-Davies) continuum model (version 3.2 from Mlawer et al., 2019). The impact of using several earlier versions of HITRAN and the continuum model on results presented here is shown in the Appendix.

It would be preferable to use line-by-line calculations; however, the computational demands of the STA calculations performed here make this prohibitive (see below). As shown in Figure 5b of Hodnebrog et al. (2013), the NBM agrees well with line-by-line calculations for the purposes of the calculations presented here. Updated line-by-line calculations will be used in the full implementation of the new method in section 5, where a quantitative comparison with the updated version of the NBM will also be presented. Sihra et al. (2001) compared the clear sky IRF from an earlier version of the NBM with a line-by-line code and found that for all but five of the 61 gases investigated, the NBM was accurate to within 4%; exceptions included halocarbons with very sharp spectral features (notably $CF_4$) and light hydrocarbons, which have much more spectral structure than most halocarbons.

To calculate the IRF in the Pinnock et al. (1995) method, a weak absorber is introduced into the model, with an absorption cross section which is constant with wavenumber. An absorption cross section of $1.0 \times 10^{-18}$

$cm^2$ $molecule^{-1}$ is used (for comparison, the peak absorption cross section for CFC-11 is about $4.5 \times 10^{-18}$ $cm^2$ $molecule^{-1}$). The weak absorber is taken to have a volume concentration of 1 ppb. For most calculations here, it is assumed to be well mixed throughout the atmosphere, but this is relaxed in section 5.

The STA uses the standard technique from Pinnock et al. (1995). By assuming that the stratosphere is in global mean radiative equilibrium in the unperturbed case, the shortwave heating rate is taken to be the same size as, but opposite sign to, the global mean longwave heating rate, at each model level. A perturbation in gas concentrations leads to a change in longwave heating rate; a simple iterative method is used to calculate the temperature change that is needed to return the longwave heating rate to its unperturbed value, to restore radiative balance. This technique is used for the global mean calculations in sections 3 and 4. In section 5, where calculations are performed for separate tropical and extratropical profiles, STA is computed using the fixed-dynamical heating (FDH) approximation (e.g., Fels et al., 1980) as the assumption of radiative equilibrium no longer holds. This method has been widely used to compute RF (e.g., Ramaswamy et al., 2019). In this case, in each latitude range, the dynamical (and solar) heating is assumed to exactly balance the unperturbed longwave radiative heating. When the weak absorber is added, this dynamical heating is assumed to remain constant and the iterative method is used to calculate the temperatures that result in the longwave radiative heating again balancing this.

The spectral variation of IRF can be calculated using just two runs of the radiation code—one with and one without the weak absorber; this is because the weak absorber only impacts the forcing in the wavenumber band in which it absorbs. The calculation of the spectral variation of RF (i.e., including STA) is much more involved and computationally demanding; as section 3 will show, as a result of the temperature change, a perturbation by a halocarbon in one spectral region influences the stratospheric emission by other gases, notably $CO_2$, $O_3$, and $H_2O$, at other wavenumbers. Hence, the resulting RF is manifested across the whole infrared region, rather than just in the band in which the halocarbon absorbs. The RF is calculated with the weak absorber in one wavenumber band only, but the STA must be performed including all other wavenumber bands, with this calculation repeated for all 300 bands in the NBM. Because the perturbation to longwave heating rates of a weak absorber in a single spectral band is so small, the calculation of precise values of RF puts more exacting requirements on convergence criteria than is the case for, for example, perturbations of $CO_2$ or CFC-11. The STA procedure is taken to have converged once the RF differs by less than $10^{-9}$ W $m^{-2}$ between iterations, and the temperature change, at any stratospheric level, is less than $10^{-8}$ K between iterations. This significantly adds to the computational burden. Although it cannot be assured that the STA calculated with the NBM will be the same as that from a line-by-line code, section 5 will note the degree of agreement with selected exploratory calculations using a line-by-line code.

A consequence of STA is that the spectrally averaged RF at the tropopause and the top of atmosphere (TOA) is equal; this is because the (global mean) stratosphere is in radiative equilibrium, and so there can be no radiative flux divergence across the stratosphere, either in the unperturbed case or after STA. The same is true when FDH is applied to separate profiles, as the radiative flux divergence must be the same in both the unperturbed and perturbed cases. This is used as a further way to monitor convergence of the STA calculations; for the cases presented here the final tropopause and TOA forcings are equal to within 0.1% and generally better than this. In contrast to RF, the ERF is defined at the TOA, so it is also useful to compare these tropopause and TOA views.

Most of the calculations presented here, which demonstrate the approach and establish its feasibility for improving the Pinnock et al. (1995) method, use a global mean profile of temperature, ozone, and clouds derived from meteorological analyses (see Freckleton et al., 1998). The tropopause is specified using the 2 K $km^{-1}$ definition, at 128.6 hPa; for STA, all pressures lower than this are adjusted. The background concentrations of other greenhouse gases are taken from Hodnebrog et al. (2013): $CO_2$ at 389 ppm, $CH_4$ at 1800 ppb, and $N_2O$ at 323 ppb.

For the final calculations presented in section 5, more accurate results are obtained by performing calculations that distinguish between tropical and extratropical atmospheres. As discussed in Freckleton et al. (1998) and Myhre et al. (2006) (see also Myhre & Stordal, 1997), such an approach can reproduce the global mean forcing calculated using much higher spatial resolution calculations, to within about 1%. As a specific example, Myhre and Stordal (1997) report errors in the global mean forcing using a single global mean profile which exceed 7%, relative to calculations performed at monthly resolution at 2.5° × 2.5° spatial

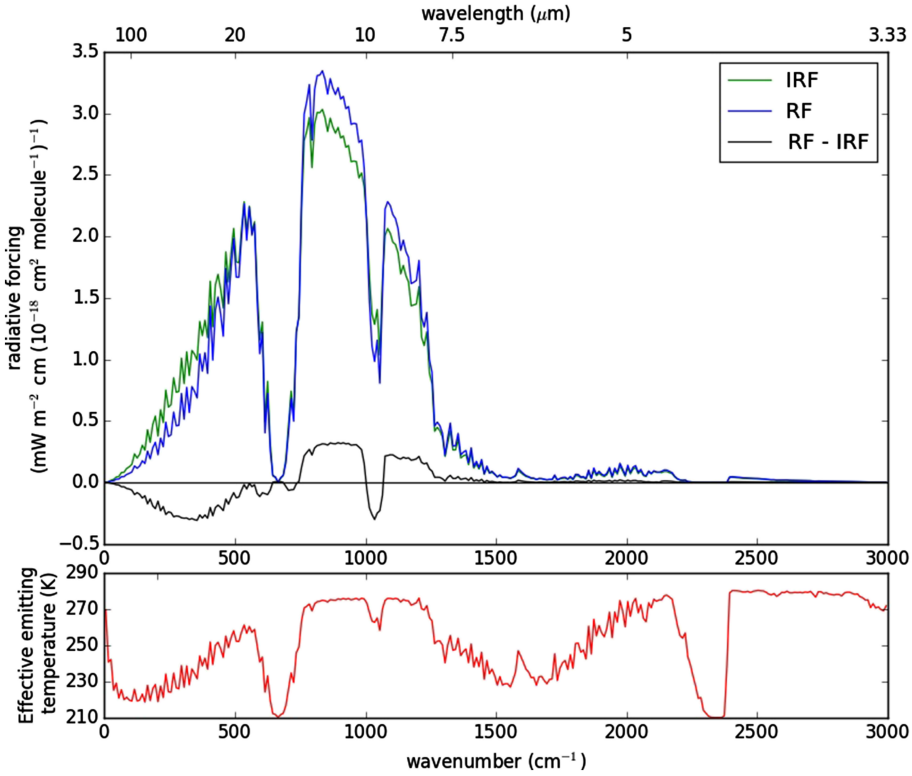


**Figure 1.** Top frame: IRF (green) and RF (blue) as a function of the wavenumber at which a weak absorber is present, for a global mean atmosphere and a 0 to 1 ppb increase in mixing ratio (see text for details). For the IRF, the forcing is entirely at that wavenumber. For the RF, the forcing shown at that wavenumber is the wavenumber-averaged forcing. The difference (RF minus IRF) is shown in black. Figure 6 shows the ratio of RF to IRF for a more refined calculation. The y-axis units in this and later figures is the spectral radiative forcing [W $m^{-2}$ $(cm^{-1})^{-1}$] per unit absorption cross section, due to the 1 ppb increase. Bottom frame: Effective emitting temperature (in K) as a function of wavenumber derived from the upward spectral irradiance at the tropopause.

resolution; these errors are reduced to less than 1% when using one tropical and one extratropical atmosphere (Myhre et al., 2006). Hence the final NBM results (see section 5), which are used to adjust updated line-by-line IRF calculations, use a three-atmosphere approach (tropics and northern and southern extratropics, with tropopause pressures at 110.9, 217.0, and 218.8 hPa, respectively, with STA calculated at all pressures below these) from Freckleton et al. (1998). Figure 5a of Hodnebrog et al. (2013) shows that this mostly impacts the RF in the 100- to 500-$cm^{-1}$ spectral region.

All discussion here uses wavenumbers, but equivalent wavelengths are indicated on figures.

## 3. Spectral Variation of Instantaneous and Adjusted Forcing

Figure 1 (upper plot) shows a principal result of this work, with the tropopause IRF and RF as a function of wavenumber, and the difference between the two. The IRF is the forcing due to the weak absorber at the given wavenumber, while the RF is the forcing due to the weak absorber at the given wavenumber *and* the impact of STA on irradiances at all wavenumbers. Where RF is less than IRF, this indicates a cooling of the lower stratosphere and where it is greater, it indicates a warming. RF is less than IRF at wavenumbers lower than about 750 $cm^{-1}$ and in the vicinity of 1,000-$cm^{-1}$ ozone band. It is otherwise positive between about 750 and 1,200 $cm^{-1}$ and weakly positive at wavenumbers greater than 1,200 $cm^{-1}$.

To connect this result to the simple conceptual model presented in section 1, the lower frame on Figure 1 shows the effective emitting temperature of the troposphere, computed from the upwelling spectral irradiance at the tropopause. This shows that, in general, wavenumbers with high effective temperature are associated with STA causing RF to exceed IRF, and vice versa. However, clearly other factors are at play. In very

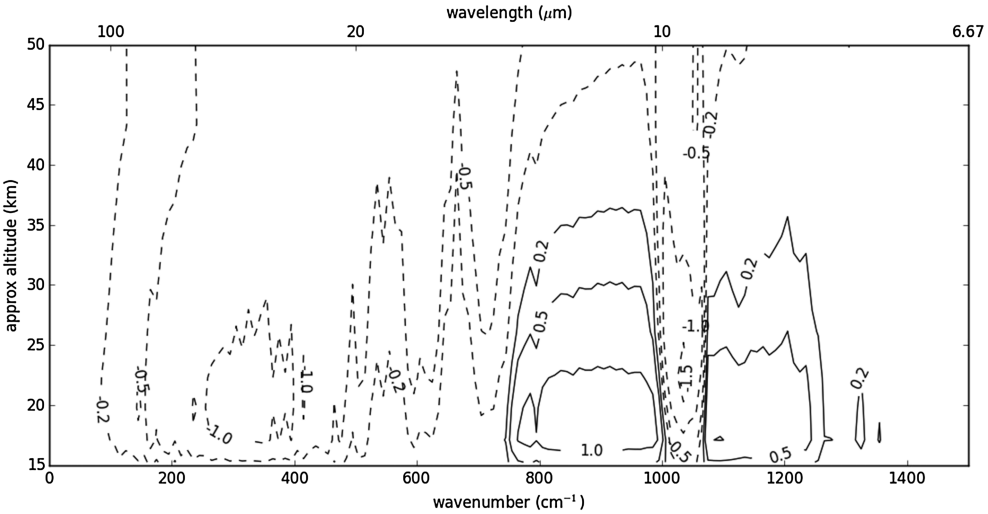


**Figure 2.** Global average stratospheric temperature change as a function of the wavenumber at which a weak absorber is introduced, for a 0 to 1 ppb increase in mixing ratio. Solid lines indicate warming, dashed lines indicate cooling. Contours at ±0.2, ±0.5, and ±1.5 mK cm $(10^{-18}$ cm$^2$ molecule$^{-1})^{-1}$. Wavenumbers greater than 1,500 cm$^{-1}$ are not shown as temperature changes are negligible.

opaque regions (notably the strong $CO_2$ absorption at 670 cm$^{-1}$) the weak absorber hardly changes that opacity, and both IRF and RF are small. In the water vapor vibration band between about 1,300 and 2,000 cm$^{-1}$, the Planck function is decreasing rapidly with wavenumber which, when combined with the relatively high opacity, leads to a very small RF and IRF due to the weak absorber.

Figure 2 shows the STA as a function of wavenumber and altitude, for wavenumbers for which there is significant temperature change. In accordance with the conceptual model discussed in section 1, in spectral regions where the effective emitting temperature is relatively low (0–750 cm$^{-1}$, and in the strong ozone bands near 1,000 cm$^{-1}$), the stratosphere cools causing RF for the weak absorber to be lower (by up to 40% at low wavenumbers) than IRF. By contrast, in the more transparent 750- to 1,200-cm$^{-1}$ region (except for the ozone bands), the lower stratosphere warms, causing RF to exceed IRF by typically 10%.

Figure 3 compares IRF at the tropopause and TOA as a function of wavenumber. This follows the spectral pattern seen in Figure 1. A positive IRF indicates a *reduction* in net upward irradiance. If the TOA IRF is higher than the tropopause IRF this indicates a convergence of irradiance in the stratosphere; this leads to a warming following STA. Therefore, in more transparent regions of the spectrum (750 to 1,200 cm$^{-1}$, excluding the ozone bands), additional stratospheric absorption reduces the upwelling irradiance from the troposphere by more than any extra stratospheric emission increases it, causing the TOA IRF to exceed the tropopause IRF. In more opaque regions at lower wavenumbers, the reverse is true and the tropopause IRF exceeds the TOA IRF, leading to a cooling following STA. In the center of the $CO_2$ 15-μm complex, the opacity is already so high that the addition of a weak gas has little impact at either TOA or tropopause, but a slight negative IRF at the TOA can be seen which is interpreted as being due to the increase in effective emitting height which, in the stratosphere, means higher temperatures. Although the spectral variation of the tropopause IRF can hint at the likely sign of the STA, Figure 3 indicates that it is ultimately the difference between the tropopause and TOA IRF that drives STA and determines its sign and magnitude.

Figure 4 shows the spectral variation of the RF (i.e., the IRF and the effect of STA) at the tropopause and TOA. As noted above, unlike the instantaneous case, where the irradiance change is solely at the wavenumber where the weak absorber is located, the RF has STA-induced components at wavenumbers away from where the weak absorber is active. Figure 4 has been drawn to emphasize this "nonlocal" forcing, with the sharp positive forcing at the wavenumber of the weak absorber indicated at the top of each frame; this differs between the tropopause and TOA (and differs from the IRF on Figure 3, due to the STA). Figure 4a shows the situation for an absorber in a wavenumber band (340–350 cm$^{-1}$) where STA leads to a cooling

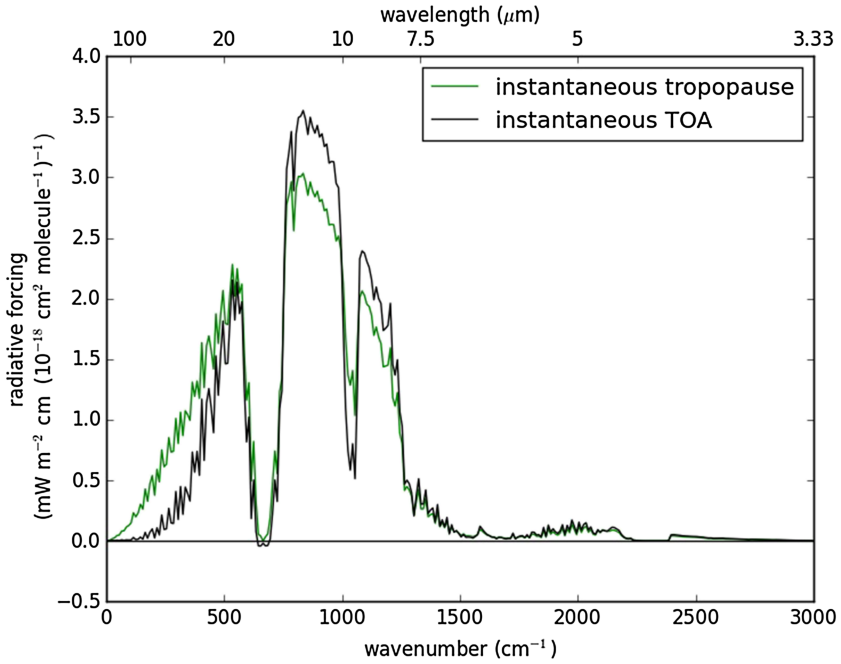


**Figure 3.** Instantaneous radiative forcing at the tropopause and top of atmosphere (TOA), as a function of the wavenumber at which a weak absorber is present, for a global mean atmosphere and a 0 to 1 ppb increase in mixing ratio.

stratosphere. The peak at 340–350 $cm^{-1}$ is 10 to 30 times greater than the responses caused by STA away from this wavenumber. The responses are primarily associated with the 15-μm $CO_2$ bands and the 9.6-μm ozone bands, plus a contribution from the strong water vapor rotation bands at lower wavenumbers. The forcing change due to STA is opposite at TOA and tropopause. At the tropopause, a stratospheric cooling leads to less emission to the troposphere which constitutes a negative forcing; at TOA, a cooling reduces the net irradiance emitted to space, which constitutes a positive forcing. So, referring to Figure 3 for a weak absorber in this wavenumber band, the tropopause RF decreases from its instantaneous value and increases from its instantaneous value at the TOA; when averaged over all wavenumbers, the tropopause and TOA RFs are identical (and given by the value shown on Figure 1), as a higher "local" forcing is compensated by negative values at other wavenumbers. These TOA forcings can be directly compared with ERFs which are also computed at the TOA. Figure 4b shows the situation for the band (850–860 $cm^{-1}$) where STA leads to a warming stratosphere; the arguments above are reversed, and the "local" forcing is two orders of magnitude greater than the responses caused by the STA away from this wavenumber band.

## 4. Using the Stratosphere-Adjusted Forcing to Estimate Halocarbon Radiative Efficiencies

Section 3 has established how STA modifies stratospheric temperature, and hence RF, for absorption in narrow spectral bands and this enables an STA-modified version of the Pinnock et al. (1995) method to be derived (Figure 1). This facilitates the calculation of the RE for specific gases, rather than just the instantaneous RE (IRE), using that method. However, to establish that this is indeed the case, the method must be tested for a range of real halocarbons to see how it compares with the RE calculated directly for that halocarbon using the NBM. Since the STA for a real halocarbon results from absorption and emission at a range of different wavenumbers, there is no guarantee that it will be the linear sum of the adjustments calculated individually for each wavenumber, as was computed in section 3.

Table 1 shows the results for a representative sample of eight halocarbons, ranging from those for which there is a relatively large increase in RE (10–12%) due to STA (CFC-11, CFC-113a, HFC-134a, HCFC-123, HCFC-22, and HFC-227ea), one which, because of strong overlap with the 9.6-μm ozone bands, has a 4%

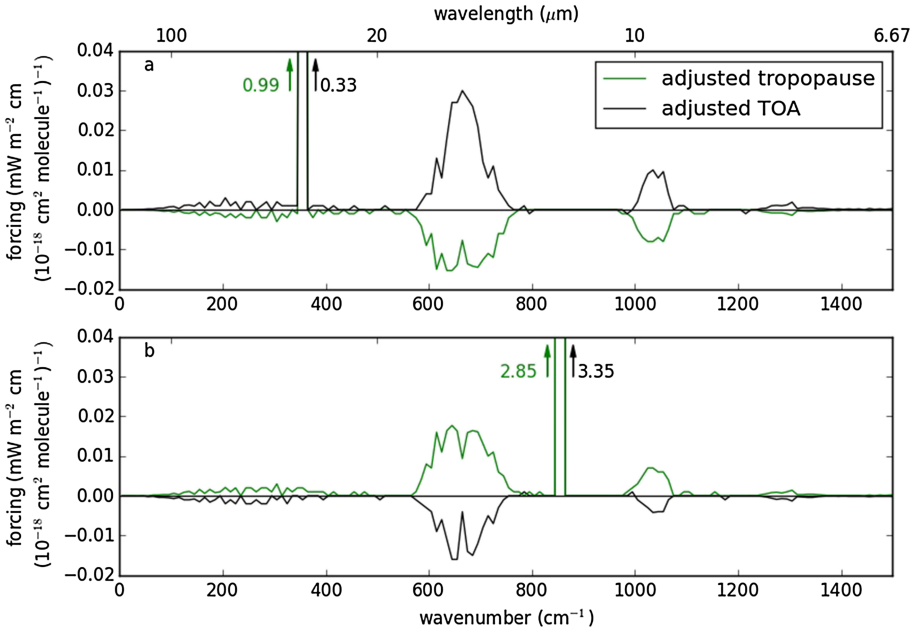


**Figure 4.** Spectrally resolved RF at the tropopause and top of atmosphere (TOA) due to a weak absorber (0 to 1 ppb increase in mixing ratio) introduced in two different 10-$cm^{-1}$ wavenumber bands. (a) Weak absorber in the 350- to 360-$cm^{-1}$ band. (b) Weak absorber in the 850- to 860-$cm^{-1}$ band. In both cases, the forcing in the band in which the weak absorber is introduced is a sharp peak which is off-scale on the y-axis. The RF for this wavenumber band is shown by the annotations (green for tropopause forcing, black for TOA forcing) at the top of each frame. The much smaller forcing at other wavenumbers is due to the stratospheric temperature adjustment impacting on emission predominantly by $CO_2$, $H_2O$, and $O_3$.

*decrease* in forcing due to STA (HFC-41) and $CF_4$ which mostly absorbs in a very narrow spectral region (around 1,280 $cm^{-1}$), for which STA is of lesser absolute importance. Table 1 shows IRE and RE directly using the NBM, IRE, and RE using the STA-modified Pinnock et al. (1995) method and the error resulting from that method. The RE error is compared with the simple 10% increase to account for STA that was assumed in Hodnebrog et al. (2013) for most compounds.

The error in applying the adjusted Pinnock method are small (less than 1.4% for all gases; Table 1, column 8). Notably these errors are of similar size to those for the IRE (Table 1, column 4) which shows that the adjusted Pinnock method works well for all gases. For most gases, the adjusted Pinnock method agrees better with the NBM than applying the simple 10% increase to crudely account for adjustment; an exception is CFC-11 where STA just happens to cause almost exactly a 10% increase. The better agreement is most notable for HFC-41 where the adjusted Pinnock method correctly predicts that STA leads to a reduction rather than an increase in forcing (see the change from IRF to RF in the vicinity of the 1,000 $cm^{-1}$ ozone bands in Figure 1).

It must be stressed that the errors in Table 1 are relative to the RE calculated for a given gas using the NBM, rather than the estimated total error. Hodnebrog et al. (2013) discuss in detail the likely uncertainties in computing the RE for halocarbons; these arise from a number of sources, including the measurement or calculation of the absorption cross sections, radiative transfer uncertainties, and uncertainties due to the specification of the atmospheric conditions. The total error was dependent on the lifetime of the gas, and whether the cross sections were measured or calculated, and were in the range 13–23%.

## 5. Updated Spectrally Varying Radiative Forcing Curve

Section 4 illustrated the robustness of the concept of including STA, using a single global mean atmosphere, using the NBM. In this section, an updated version of the Pinnock et al. (1995) method is presented which improves on the use of the global mean atmosphere and incorporates updated line-by-line calculations.

**Table 1**
*Radiative Efficiencies (RE) (in W $m^{-2}$ $ppb^{-1}$) for Eight Selected Halocarbons*

| | Instantaneous radiative efficiency | | | Radiative efficiency | | | |
|---|---|---|---|---|---|---|---|
| | NBM | Pinnock method | Error in Pinnock method (%) | NBM | Pinnock method | Error in Pinnock method (%) | Error assuming 10% adjustment |
| CFC-11 | 0.251 | 0.249 | −0.8 | 0.277 | 0.274 | −1.08 | −0.03 |
| CFC-113a | 0.218 | 0.216 | −0.93 | 0.243 | 0.240 | −1.25 | −2.27 |
| HFC-134a | 0.157 | 0.155 | −1.29 | 0.175 | 0.173 | −1.16 | −2.64 |
| HCFC-22 | 0.202 | 0.200 | −1.00 | 0.224 | 0.221 | −1.36 | −1.82 |
| HCFC-123 | 0.182 | 0.180 | −1.01 | 0.202 | 0.200 | −1.26 | −2.02 (−5.4%) |
| HFC-227ea | 0.238 | 0.236 | −0.85 | 0.266 | 0.263 | −1.14 | −2.46 |
| HFC-41 | 0.0263 | 0.0260 | −1.15 | 0.0250 | 0.0247 | −1.21 | 11.44 |
| $CF_4$ | 0.0812 | 0.0811 | −0.12 | 0.0889 | 0.0888 | −0.11 | −0.35 |

*Note*. The first three columns compare the instantaneous RE calculated using the NBM and the Pinnock et al. (1995) method (as updated in this paper) and the percentage error in the latter. The next three columns show the same but including stratospheric temperature adjustment in the Pinnock et al. (1995) method. The final column shows the error using the simple Hodnebrog et al. (2013) assumption, whereby the RE is 10% higher than the instantaneous RE. The value in parentheses for HCFC-123 is the error assuming a 6.5% correction for that gas, as was done in Hodnebrog et al. (2013), based on earlier simulations.

The NBM calculations presented above were repeated using three atmospheres, one representative of the tropics and one each for the southern and northern hemisphere extratropics (as, when combined, these provide a better estimate of the true global mean, see section 2). Figure 5 shows the difference between the single and three atmosphere approaches, for the RF when incorporating STA. This is similar to that found for instantaneous RF in Hodnebrog et al. (2013). Figure 5 also shows the calculations for the tropical and

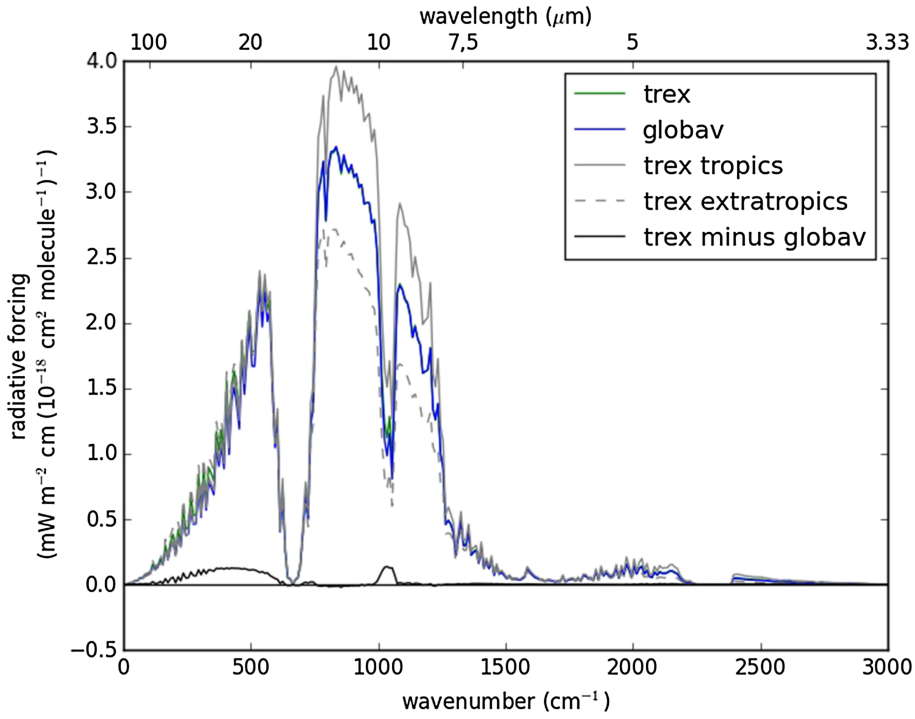


**Figure 5.** RF as a function of the wavenumber at which a weak absorber is present, for a 0 to 1 ppb increase in mixing ratio (see text for details). The blue curve (globav) shows the calculation using a single global mean profile (and is identical to the blue curve on Figure 1). The green curve (trex) shows the global mean calculated using three profile representing tropical and extratropical atmospheres; the gray solid and dashed curves show the calculations separately for the tropical and extratropical (average of northern and southern hemisphere) profiles, respectively. The black curve shows the difference (trex minus globav). The forcing shown at a particular wavenumber is the wavenumber-averaged forcing due to the presence of the weak absorber at the given wavenumber.

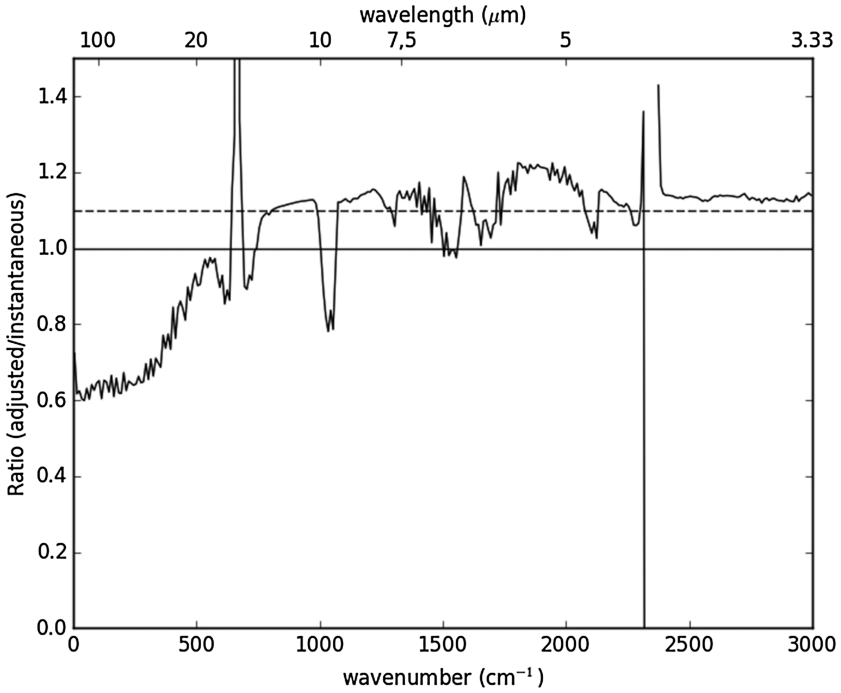


**Figure 6.** Ratio of the RF to the IRF at the tropopause as a function of the wavenumber at which a weak absorber is present. The strong features at around 670 and 2,350 $cm^{-1}$ are coincident with strong $CO_2$ absorption bands, where the IRF due to the weak absorber is very close to zero. The dashed horizontal line at a ratio of 1.1 is shown to indicate the assumption used for most gases in Hodnebrog et al. (2013).

extratropical atmospheres separately (the northern and southern hemisphere extratropics cases are so similar that their average is shown). This illustrates that the tropical and extratropics cases differ significantly in the 750- to 1,350-$cm^{-1}$ region, but the average of these profiles is relatively close to the global average curve. The main differences between the single global mean atmosphere and the mean of the three profiles is in the ozone band near 1,000 $cm^{-1}$ and in the water vapor rotation bands at wavenumbers less than 600 $cm^{-1}$

Figure 6 shows the ratio of the RF and IRF. This echoes the absolute differences shown on Figure 1 and emphasizes the relative importance of the change. The sharp features at around 670 and 2,350 $cm^{-1}$ are where RF is in any case essentially zero due to the strong $CO_2$ absorption features. The difference between the main $CO_2$ and $O_3$ bands is caused by the contrast in effective emitting height, being in the mesosphere at the center of the $CO_2$ bands and in the stratosphere for $O_3$. Figure 5 also shows the 10% adjustment used for most gases in Hodnebrog et al. (2013). It indicates that this was a reasonable assumption, on average, between 750 and 1,600 $cm^{-1}$, but with notable deviations.

Line-by-line (LBL) calculations of the spectrally varying RF that were introduced in Hodnebrog et al. (2013) are inherently more accurate than NBM calculations and are at a higher spectral resolution. As noted in section 1, it was not computationally practicable to generate the spectrally varying RF incorporating STA using an LBL. Hence, we choose to combine the effect of STA from the NBM (i.e., the ratios shown in Figure 6) with updated LBL IRF calculations to provide our final updated values for the Pinnock et al. (1995) method. There will be some level of approximation in applying the lower resolution STA effect with the high-resolution LBL output (see below), but the impact of this is expected to be minor when applied to realistic halocarbons with wide spectral features.

The Oslo line-by-line model (OLBL) used in Hodnebrog et al. (2013) incorporated the CKD0 water vapor continuum. As discussed in Etminan et al. (2016), see Appendix 1, more recent versions lead to a significant impact on RF in some spectral regions. The calculations here use CKD-2.4.1, which alleviates most of the differences between older versions of CKD and the most recent version, MT_CKD-3.1 (Figure A2). There are further small updates to the treatment of clouds in the OLBL. The OLBL calculations are performed using the two atmosphere (tropical/extratropical) approach discussed in Hodnebrog et al. (2013); the

weak absorber is perturbed from 0 to 0.1 ppbv (a perturbation is appropriate for present-day observed concentrations of halocarbons) and scaled up to 1 ppbv to produce the RF. The 0.02 $cm^{-1}$ resolution output of the OLBL is averaged to 1 and 10 $cm^{-1}$ resolution for the purposes of updating the Pinnock method.

A number of exploratory calculations of STA had been performed with an older version of the OLBL, with the weak absorber imposed in 10 $cm^{-1}$ intervals; these helped motivate the work presented here. Computational constraints meant it was not possible to achieve full convergence of the OLBL STA calculations nor perform them over the entire spectral range covered here. Nevertheless, these do allow some comparison with the NBM results. As an example, we present results for three spectral bands (1,000–1,010, 1,030–1,040, and 1,200–1,210 $cm^{-1}$) for which the adjusted/instantaneous ratio varies quite strongly. For the NBM these ratios were 0.99, 0.78, and 1.15, respectively, while for the OLBL, the ratios were 1.00, 0.82, and 1.12, respectively. These results provide some reassurance that the STA in the NBM behaves in a closely similar way to the OLBL.

The adjusted/instantaneous ratio derived at 10 $cm^{-1}$ using the NBM is linearly interpolated on to a 1 $cm^{-1}$ grid. A refinement is applied near the center of the 15-μm $CO_2$ bands. The large adjusted/instantaneous ratio shown on Figure 6 occupies the whole of the 660- to 670-$cm^{-1}$ NBM band. In reality, the strongest $CO_2$ lines occupy a much narrower spectral region (about 667.5 to 670 $cm^{-1}$); simple linear interpolation from the NBM 10-$cm^{-1}$ grid to 1 $cm^{-1}$ would cause this strong region to incorrectly influence the ratio for all wavenumbers between 655.5 and 674.5 $cm^{-1}$. Instead, the highest ratio found at 10-$cm^{-1}$ resolution (27.7) is applied only to the narrow spectral region, and then a ratio of 1.3, typical of the neighboring NBM bands, is applied at all other wavenumbers between 655.5 and 674.5 $cm^{-1}$. In practice, this refinement has little impact on most halocarbons; however, molecules with carbon-bromine bonds generally have strong features in the vicinity of the 15-μm $CO_2$ bands.

Figure 7a compares the IRF from the OLBL, with the OLBL results in Hodnebrog et al. (2013) at 1-$cm^{-1}$ resolution. The differences are largely consistent with those expected from the change in version of the water vapor continuum (see Appendix Figure A2).

Figure 7b shows the impact of including the STA derived from the NBM to the OLBL results at 1-$cm^{-1}$ resolution—the outcome is, by design, consistent with Figure 1, which is the NBM equivalent, albeit at a higher spectral resolution. Figure 7c shows the same, but averaged to 10-$cm^{-1}$ resolution, which makes differences clearer in regions of high spectral variation. Figure 7d shows a comparison of the IRF computed using the OLBL (averaged to 10-$cm^{-1}$ resolution) and the NBM. Throughout most of the region where the RF is high (250–1,400 $cm^{-1}$), the NBM agrees with the OLBL to 5% or better, except in some isolated wavenumber bands on the edge of the 15-μm $CO_2$ bands where the forcing is in any case small. Comparison with the other frames of Figure 7 shows that the OLBL-NBM differences are as small as the effect of the OLBL updates (Figure 7a) and much smaller than the impact of STA (Figures 7b and 7c) which gives further confidence in the STA calculated using the NBM.

The results shown in Figures 7b and 7c can be used to calculate the RE of a gas, given the wave number-dependent absorption cross section by applying the Pinnock et al. (1995) method. The RE is given by

$$RE = \sum_i F_i \sigma_i \Delta\upsilon, \tag{1}$$

where $F_i$ is the spectrally resolved radiative forcing per unit cross section W $m^{-2}$ cm $(cm^2\ molecule^{-1})^{-1}$ in waveband $i$ shown in Figures 7b and 7c and $\sigma_i$ is the absorption cross section in waveband $i$ [$cm^2\ molecule^{-1}$] averaged over the wavenumber increment $\Delta\upsilon$ [$cm^{-1}$]. The values of $F_i$ for the wavenumbers 0–3,000 $cm^{-1}$ are given in the supporting information; this includes OLBL IRF and NBM RF/IRF ratios and their combined values for $\Delta\upsilon$ = 1 and 10 $cm^{-1}$. Hodnebrog et al. (2013) show that while, for most gases, calculating the RE using 10 $cm^{-1}$ rather than 1-$cm^{-1}$ resolution commits an error smaller than 2%, for some gases the error can reach 8%.

As detailed in Hodnebrog et al. (2013), calculations of RE must account for the fact that halocarbons deviate from being well mixed in the atmosphere, which has been assumed in the calculations for the Pinnock et al. (1995) method here; the impact of this deviation depends on the lifetime (and, in principle, the location of the emissions for particularly short-lived species).

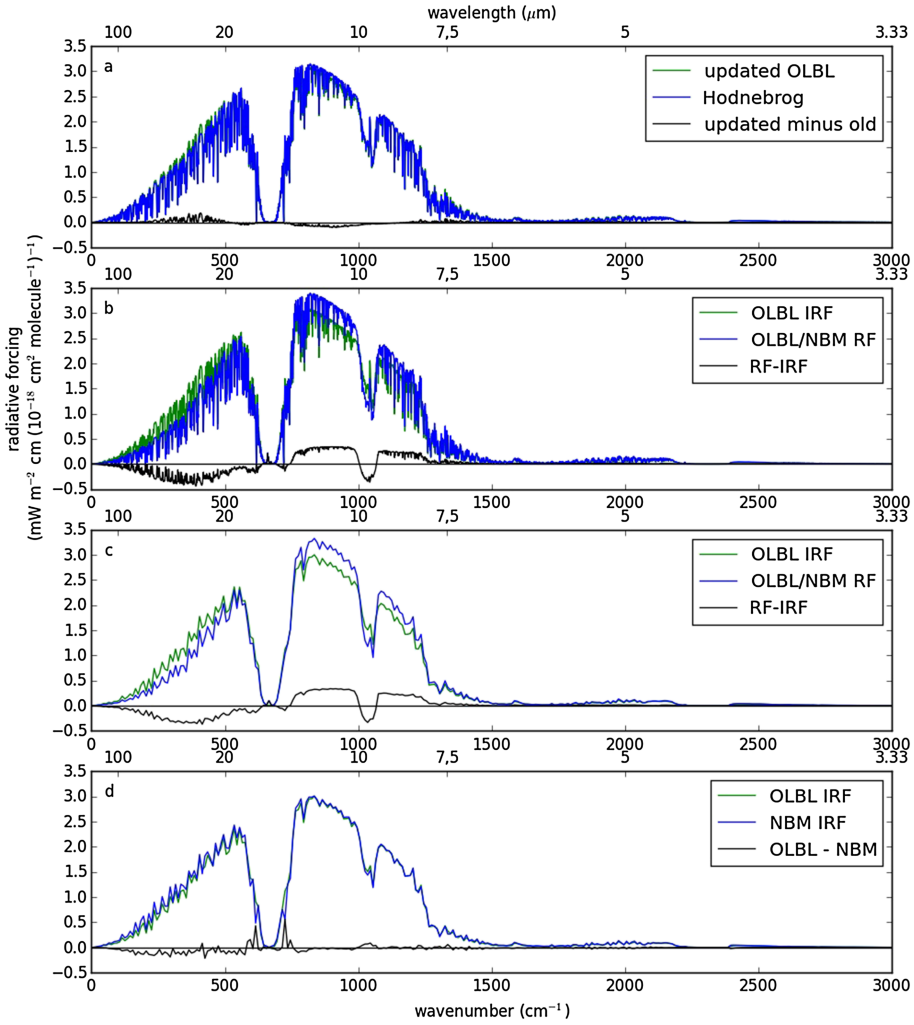


**Figure 7.** IRF and RF as a function of the wavenumber at which a weak absorber is present, for a 0 to 1 ppb increase in mixing ratio (see text for details). (a) Updated Oslo line-by-line model (OLBL) IRF averaged to 1 $cm^{-1}$ resolution, compared to OLBL calculations presented in Hodnebrog et al. (2013) and their difference. (b) Updated OLBL IRF shown in Panel (a) and RF using the OLBL IRF and the NBM RF/IRF ratio interpolated to 1 $cm^{-1}$ resolution and the absolute difference between these. (c) As (b) but averaged to 10 $cm^{-1}$ resolution. (d) IRF calculated by the OLBL (averaged to 10 $cm^{-1}$ resolution) and the NBM and the absolute difference between these. The RF shown at a given wavenumber is the wave number-averaged forcing due to the presence of the weak absorber at the given wavenumber.

Hodnebrog et al. (2013) developed simple corrections for this, based on chemical transport model simulations and radiative transfer calculations using the Oslo Broadband Model. These corrections should also be applied here; it is important to note that those radiative transfer calculations incorporated the impact of STA. Hence, they are directly applicable to the STA-corrected values of the Pinnock et al. (1995) method presented here. One correction applies to gases whose prime loss mechanism is photolysis in the stratosphere, so that the fractional correction to the RE is $f(\tau) = 1–0.1826\ \tau^{-0.3339}$ and is applicable for lifetimes $\tau$ in the range $10 < \tau < 10^4$ years. The second correction applies where the prime loss mechanism is tropospheric OH. In this case, $f(\tau) = 2.962\tau^{0.9312}/(1 + 2.994\tau^{0.9302})$ for $10^{-4} < \tau < 10^4$ years. For compounds with $\tau \geq 10^4$ years, it was recommended that no correction be applied.

## 6. Conclusions

This paper has examined how the stratospheric temperature adjustment due to the radiative forcing of greenhouse gases for gases at low concentrations (ppb and below) varies with the wavelength at which it

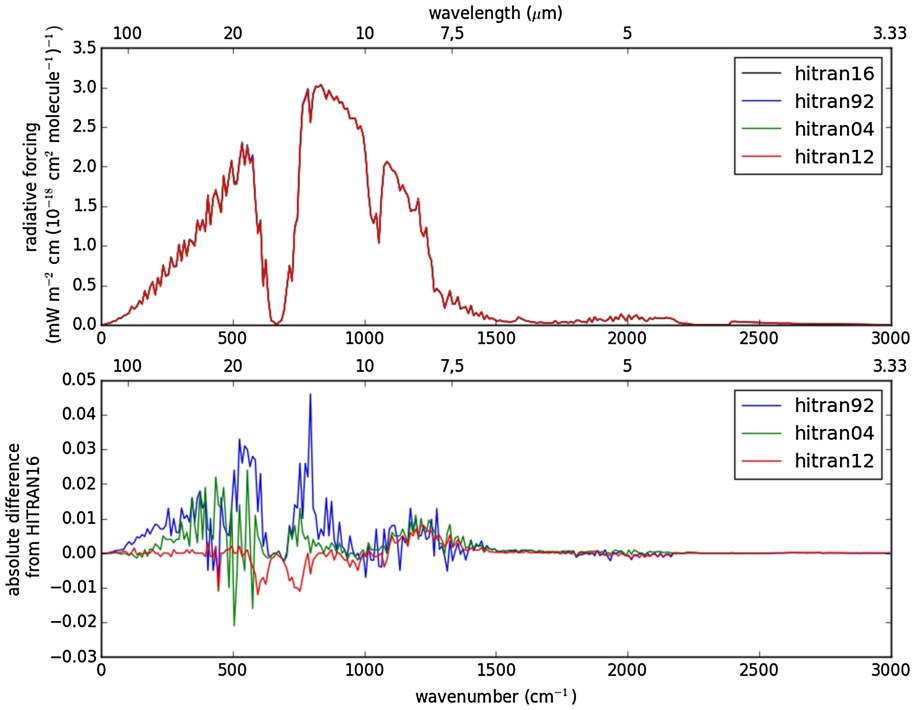


**Figure A1.** Top: IRF as a function of wavenumber at which a weak absorber is present, for a global mean atmosphere and a 0 to 1 ppb increase in mixing ratio (see text for details) for different versions of the HITRAN database (1992, 2004, 2012, and 2016). Bottom: Absolute difference relative to HITRAN16 (HITRANxx minus HITRAN). The MT_CKD3.2 water vapor continuum is used in all cases.

absorbs. Since stratospheric temperature adjustment can be an important component of rapid adjustments incorporated in the definition of effective radiative forcing, the results are also relevant to that framework.

The calculations demonstrate that increased concentrations of gases that absorb in more opaque regions of the spectrum, notably at wavenumbers less than 750 $cm^{-1}$, and in the ozone bands near 1,000 $cm^{-1}$, act to cool the lower stratosphere; hence RF (calculated at the tropopause) is up to 40% less than its instantaneous value. The opposite is true in the less opaque window region between 750 and 1,200 $cm^{-1}$ (excepting the region near 1,000 $cm^{-1}$), where enhancements of instantaneous RF are typically 10%. This relative effect persists at higher wavenumbers up to 3,000 $cm^{-1}$, but the forcing due to gases absorbing in this spectral region is, in any case, small.

The results of this work are directly applicable to an enhancement of the Pinnock et al. (1995) method, which is a widely used simplified method, based on detailed radiative transfer calculations. This enables the radiative efficiency (RE) of halocarbons and related molecules which are in their weak limit in the atmosphere, to be computed directly from laboratory or theoretical absorption cross sections, without the need for a radiative transfer code. Previous applications of the method (Hodnebrog et al., 2013) have recommended a very simple generic increase in RE by 10% to account for stratospheric temperature adjustment and thus essentially ignored the wavenumber dependence of this correction. It is demonstrated here that applying a wavenumber-dependent correction to the Pinnock et al. (1995) allows the RE from detailed calculations to be reproduced to better than 1.5% for the gases tested here. The correction does not make the application of the Pinnock et al. (1995) method any more complicated. In future it may be possible to explore the role of stratospheric temperature adjustment in more detail, by employing a line-by-line code, with the weak absorber constrained to even narrower spectral intervals, and with expanded horizontal resolution; it may also be possible to consider inclusion of rapid responses beyond stratospheric temperature adjustment.

Our final recommended values for the Pinnock et al. (1995) method use updated line-by-line calculations modified by the wavenumber-dependent correction for stratospheric temperature adjustment from the NBM. These values are available in the supporting information. A separate paper will provide updated

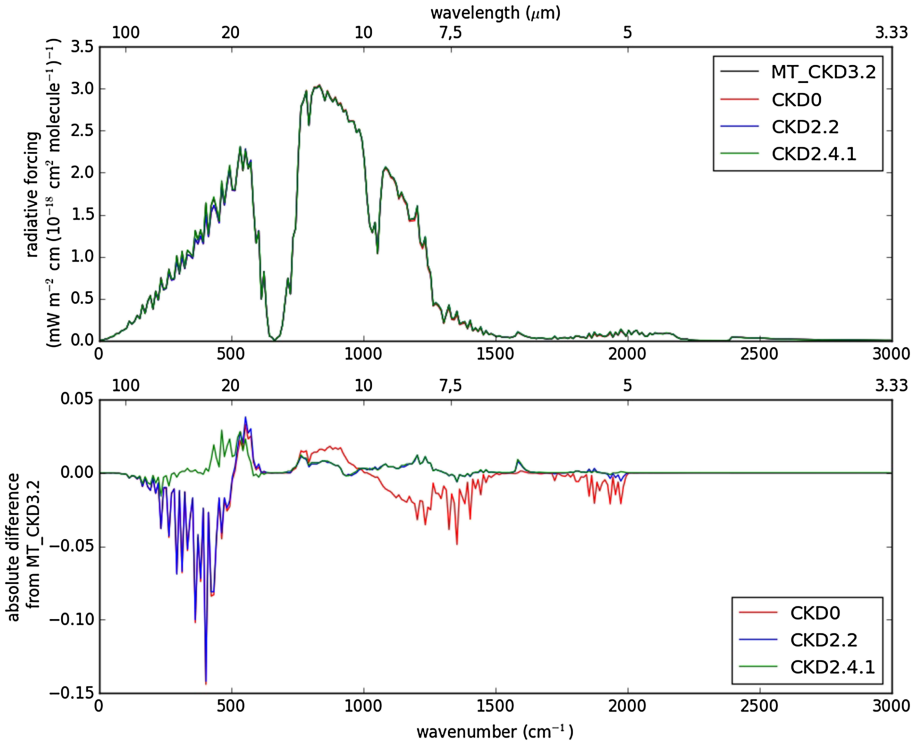


**Figure A2.** Top: IRF as a function of the wavenumber at which a weak absorber is present, for a global mean atmosphere and a 0 to 1 ppb increase in mixing ratio (see text for details) for four different versions of the CKD or MT_CKD water vapor continuum (CKD0, CKD2.2, CKD2.41, and MT_CKD3.2). Bottom: Absolute difference relative MT_CKD3.2 (CKDxx minus MT_CKD3.2). HITRAN16 is used in all cases. Where CKD2.2 cannot be seen in the bottom frame, it is identical to CKD2.4.1.

REs and associated emissions metrics (such as the GWP) for a wide range of halocarbons and related molecules, expanding on the work of Hodnebrog et al. (2013).

### Data Availability Statement

The new updated values for the updated Pinnock et al. (1995) method are presented in a spreadsheet as part of the supporting information. These data are also deposited on the University of Reading Research Data Archive: (Shine & Gunnar, 2020).

## Appendix A: Impact of Changes in Spectroscopic Databases and Water Vapor Continuum Formulation

This Appendix briefly assesses the dependence of halocarbon RE to updates to both the HITRAN database (see Gordon et al., 2017 for references to earlier versions) and the MT_CKD (and its predecessor CKD) continuum (Mlawer et al., 2012). This is not meant to be exhaustive (not all versions are included) but is nevertheless indicative. Among others, Lu et al. (2012) and Zhu et al. (2019) have explored the impact of different HITRAN databases on calculations of infrared irradiances. For reference, the line-by-line calculations in Hodnebrog et al. (2013) used HITRAN08 and CKD0.

Figure A1 shows the impact of various different versions of HITRAN and the differences relative to HITRAN16. Figure A2 shows the impact of different versions of CKD and MT_CKD and the difference relative to MT_CKD3.2. The top frame in both figures indicates that the impact of updates on halocarbon forcing is small, and generally, no more than a few percent at any one wavenumber.

Table A1 shows the effect of using these different versions on the RE for selected halocarbons. For a few cases that were tested, the differences due to the application of older versions of HITRAN and CKD are approximately additive. The largest impact is seen for $CF_4$, for which absorption predominantly occurs in

**Table A1**
*Impact of Different Versions of HITRAN and the CKD/MT_CKD Water Vapor Continuum on Calculations of the Instantaneous Radiative Efficiency for Seven Selected Halocarbons Using the Updated Pinnock et al. (1995) Method*

| | HITRAN16 MT_CKD3.2 | HITRAN version % error | | | CKD/MT_CKD version % error | | |
|---|---|---|---|---|---|---|---|
| | W $m^{-2}$ $ppb^{-1}$ | 1992 | 2004 | 2012 | CKD0 | CKD2.2 | CKD2.4.1 |
| CFC-11 | 0.249 | 0.25 | 0.04 | −0.02 | 0.33 | 0.25 | 0.25 |
| CFC-113a | 0.216 | 0.52 | 0.35 | 0.26 | −0.57 | 0.43 | 0.44 |
| HFC-134a | 0.155 | 0.40 | 0.39 | 0.31 | −1.24 | 0.33 | 0.35 |
| HCFC-22 | 0.200 | 0.38 | 0.22 | 0.11 | −0.47 | 0.20 | 0.21 |
| HFC-227ea | 0.236 | 0.32 | 0.49 | 0.40 | −1.60 | 0.39 | 0.40 |
| HFC-41 | 0.0260 | 0.06 | 0.09 | −0.05 | −0.27 | 0.22 | 0.21 |
| $CF_4$ | 0.0811 | 1.02 | 0.81 | 1.13 | −3.17 | 0.42 | 0.41 |

*Note*. The absolute radiative efficiency is shown for HITRAN16 and MT_CKD3.2 (as in Table 1), with the percentage error shown when using either an older HITRAN or CKD/MT_CKD version instead.

a narrow spectral region (1,250 and 1,290 $cm^{-1}$); the largest effect is seen for the use of CKD0, for which the $CF_4$ RE was 3% lower, echoing a larger effect found for methane radiative forcing in the same spectral region (Etminan et al., 2016). HFC-134a and HFC-227ea have errors in excess of 1% using CKD0 as they have much of their absorption in the 1,100- to 1,500-$cm^{-1}$ region which was modified significantly in later versions of the continuum. Apart from this, all other errors are less than 1%; this is much less than the estimated uncertainty in the halocarbon absorption cross sections themselves, which was estimated by Hodnebrog et al. (2013) to be 5% for experimentally determined cross sections and 10% for those calculated using ab initio methods.

**Acknowledgments**
KPS thanks Kyriacos Costa for performing initial calculations exploring the possibility of incorporating STA in the Pinnock et al. (1995) method. Øivind Hodnebrog is thanked for his input on the performance of the new method. GM acknowledges funding from the Norwegian Environment Agency. We thank the reviewers and Editor Robert Pincus for many helpful suggestions.

## References

Boucher, O., Randall, D., Artaxo, P., Bretherton, C., Feingold, G., Forster, P., et al. (2013). Clouds and aerosols. In T. F. Stocker, D. Qin, G. K. Plattner, M. Tignor, S. K. Allen, J. Boschung, A. Nauels, Y. Xia, V. Bex, & P. M. Midgley (Eds.), *Climate change 2013: The physical science basis. Contribution of Working Group I to the Fifth Assessment Report of the Intergovernmental Panel on Climate Change*, (pp. 571–658). Cambridge, United Kingdom and New York, NY, USA: Cambridge University Press. https://doi.org/10.1017/cbo9781107415324.016

Etminan, M., Myhre, G., Highwood, E. J., & Shine, K. P. (2016). Radiative forcing of carbon dioxide, methane, and nitrous oxide: A significant revision of the methane radiative forcing. *Geophysical Research Letters*, *43*, 12,614–12,623. https://doi.org/10.1002/2016gl071930

Fels, S. B., Mahlman, J. D., Schwarzkopf, M. D., & Sinclair, R. W. (1980). Stratospheric sensitivity to perturbations in ozone and carbon dioxide: Radiative and dynamical response. *Journal of the Atmospheric Sciences*, *37*, 2265–2297. https://doi.org/10.1175/1520-0469(1980)037<2265:SSTPIO>2.0.CO;2

Forster, P. M., Richardson, T., Maycock, A. C., Smith, C. J., Samset, B. H., Myhre, G., et al. (2016). Recommendations for diagnosing effective radiative forcing from climate models for CMIP6. *Journal of Geophysical Research: Atmospheres*, *121*, 12,460–12,475. https://doi.org/10.1002/2016jd025320

Freckleton, R., Highwood, E., Shine, K., Wild, O., Law, K., & Sanderson, M. (1998). Greenhouse gas radiative forcing: Effects of averaging and inhomogeneities in trace gas distribution. *Quarterly Journal of the Royal Meteorological Society*, *124*(550), 2099–2127. https://doi.org/10.1256/smsqj.55013

Gamache, R. R., Roller, C., Lopes, E., Gordon, I. E., Rothman, L. S., Polyansky, O. L., et al. (2017). Total internal partition sums for 166 isotopologues of 51 molecules important in planetary atmospheres: Application to HITRAN2016 and beyond. *Journal of Quantitative Spectroscopy & Radiative Transfer*, *203*, 70–87. https://doi.org/10.1016/j.jqsrt.2017.03.045

Godin, P. J., Johnson, H., Piunno, R., Le Bris, K., & Strong, K. (2019). Conformational analysis and global warming potentials of 1,1,1,2,3,3-hexafluoropropane and 1,1,2,2,3-pentafluoropropane from absorption spectroscopy. *Journal of Quantitative Spectroscopy & Radiative Transfer*, *225*, 337–350. https://doi.org/10.1016/j.jqsrt.2019.01.003

Gordon, I. E., Rothman, L. S., Hill, C., Kochanov, R. V., Tan, Y., Bernath, P. F., et al. (2017). The HITRAN2016 molecular spectroscopic database. *Journal of Quantitative Spectroscopy and Radiation Transfer*, *203*, 3–69. https://doi.org/10.1016/j.jqsrt.2017.06.038

Hodnebrog, O., Etminan, M., Fuglestvedt, J. S., Marston, G., Myhre, G., Nielsen, C. J., et al. (2013). Global warming potentials and radiative efficiencies of halocarbons and related compounds: A comprehensive review. *Reviews of Geophysics*, *51*, 300–378. https://doi.org/10.1002/rog.20013

Huang, Y., & Wang, Y. (2019). How does radiation code accuracy matter? *Journal of Geophysical Research: Atmospheres*, *124*, 10,742–10,752. https://doi.org/10.1029/2019JD030296

Lu, P., Zhang, H., & Jing, X. W. (2012). The effects of different HITRAN versions on calculated long-wave radiation and uncertainty evaluation. *Acta Meteorologica Sinica*, *26*(3), 389–398. https://doi.org/10.1007/s13351-012-0310-1

Mlawer, E. J., Payne, V. H., Moncet, J. L., Delamere, J. S., Alvarado, M. J., & Tobin, D. C. (2012). Development and recent evaluation of the MT_CKD model of continuum absorption. *Philosophical Transactions of the Royal Society a-Mathematical Physical and Engineering Sciences*, *370*(1968), 2520–2556. https://doi.org/10.1098/rsta.2011.0295

Mlawer, E. J., Turner, D. D., Paine, S. N., Palchetti, L., Bianchini, G., Payne, V. H., et al. (2019). Analysis of water vapor absorption in the far-infrared and submillimeter regions using surface radiometric measurements from extremely dry locations. *Journal of Geophysical Research: Atmospheres*, *124*, 8134–8160. https://doi.org/10.1029/2018jd029508

Myhre, G., Shindell, D., Bréon, F.-M., Collins, W., Fuglestvedt, J., Huang, J., et al. (2013). Anthropogenic and natural radiative forcing. In T. F. Stocker, D. Qin, G. K. Plattner, M. Tignor, S. K. Allen, J. Boschung, A. Nauels, Y. Xia, V. Bex, & P. M. Midgley (Eds.), *Climate change 2013: The physical science basis. Contribution of Working Group I to the Fifth Assessment Report of the Intergovernmental Panel on Climate Change*, (pp. 659–740). Cambridge, United Kingdom and New York, NY, USA: Cambridge University Press. https://doi.org/10.1017/cbo9781107415324.018

Myhre, G., & Stordal, F. (1997). Role of spatial and temporal variations in the computation of radiative forcing and GWP. *Journal of Geophysical Research*, *102*(D10), 11,181–11,200. https://doi.org/10.1029/97jd00148

Myhre, G., Stordal, F., Gausemel, I., Nielsen, C. J., & Mahieu, E. (2006). Line-by-line calculations of thermal infrared radiation representative for global condition: CFC-12 as an example. *Journal of Quantitative Spectroscopy and Radiation Transfer*, *97*(3), 317–331. https://doi.org/10.1016/j.jqsrt.2005.04.015

Papanastasiou, D. K., Beltrone, A., Marshall, P., & Burkholder, J. B. (2018). Global warming potential estimates for the $C_1$-$C_3$ hydrochlorofluorocarbons (HCFCs) included in the Kigali Amendment to the Montreal Protocol. *Atmospheric Chemistry and Physics*, *18*(9), 6317–6330. https://doi.org/10.5194/acp-18-6317-2018

Pinnock, S., Hurley, M., Shine, K., Wallington, T., & Smyth, T. (1995). Radiative forcing of climate by hydrochlorofluorocarbons and hydrofluorocarbons. *Journal of Geophysical Research*, *100*(D11), 23,227–23,238. https://doi.org/10.1029/95JD02323

Ramaswamy, V., Collins, W., Haywood, J., Lean, J., Mahowald, N., Myhre, G., et al. (2019). Radiative forcing of climate: the historical evolution of the radiative forcing concept, the forcing agents and their quantification, and applications. *Meteorological Monographs*, *59*, 14101. https://doi.org/10.1175/AMSMONOGRAPHS-D-19-0001.1

Rind, D., & Lacis, A. (1993). The role of the stratosphere in climate change. *Surveys in Geophysics*, *14*(2), 133–165. https://doi.org/10.1007/bf02179221

Sherwood, S. C., Bony, S., Boucher, O., Bretherton, C., Forster, P. M., Gregory, J. M., & Stevens, B. (2015). Adjustments in the forcing-feedback framework for understanding climate change. *Bulletin of the American Meteorological Society*, *96*(2), 217–228. https://doi.org/10.1175/bams-d-13-00167.1

Shine, K. (1991). On the cause of the relative greenhouse strength of gases such as the halocarbons. *Journal of the Atmospheric Sciences*, *48*(12), 1513–1518. https://doi.org/10.1175/1520-0469(1991)048<1513:OTCOTR>2.0.CO;2

Shine, K., & Gunnar, M. (2020). Improved method for rapid calculation of halocarbon radiative forcing. University of Reading. Dataset. https://doi.org/10.17864/1947.240

Shine, K. P., Derwent, R. G., Wuebbles, D. J., & Morcrette, J.-J. (1990). Radiative forcing of climate. In J. T. Houghton, G. J. Jenkins, & J. J. Ephraums (Eds.), *Climate change: The IPCC scientific assessment*, (pp. 41–68). Cambridge: Cambridge University Press.

Sihra, K., Hurley, M. D., Shine, K. P., & Wallington, T. J. (2001). Updated radiative forcing estimates of 65 halocarbons and nonmethane hydrocarbons. *Journal of Geophysical Research*, *106*(D17), 20,493–20,505. https://doi.org/10.1029/2000JD900716

Smith, C. J., Kramer, R. J., Myhre, G., Forster, P. M., Soden, B. J., Andrews, T., et al. (2018). Understanding rapid adjustments to diverse forcing agents. *Geophysical Research Letters*, *45*, 12,023–12,031. https://doi.org/10.1029/2018gl079826

Zhu, M., Zhang, F., Li, W., Wu, Y., & Xu, N. (2019). The impact of various HITRAN molecular spectroscopic databases on infrared radiative transfer simulation. *Journal of Quantitative Spectroscopy and Radiation Transfer*, *234*, 55–63. https://doi.org/10.1016/j.jqsrt.2019.04.031